UC Santa Barbara

UC Santa Barbara Previously Published Works

Title

Metal-Metal Bonding as an Electrode Design Principle in the Low-Strain Cluster Compound LiScMo$_3$O$_8$

Authors

Wyckoff, Kira E
Kaufman, Jonas L
Baek, Sun Woong
et al.

Metal-Metal Bonding as an Electrode Design Principle in the Low-Strain Cluster Compound LiScMo$_3$O$_8$

Kira E. Wyckoff,[†] Jonas L. Kaufman,[†] Sun Woong Baek,[‡] Christian Dolle,[¶]

Joshua J. Zak,[§] Jadon Bienz,[∥] Linus Kautzsch,[†] Rebecca C. Vincent,[†]

Arava Zohar,[†] Kimberly A. See,[§] Yolita M. Eggeler,[¶] Laurent Pilon,[‡,⊥]

Anton Van der Ven,[*,†] and Ram Seshadri[*,†,∥]

[†]*Materials Department and Materials Research Laboratory*

University of California, Santa Barbara, California 93106, United States

[‡]*Mechanical and Aerospace Engineering Department*

Henry Samueli School of Engineering and Applied Science

University of California, Los Angeles, CA 90095, USA

[¶]*Laboratory for Electron Microscopy, Microscopy of Nanoscale Structures and Mechanisms*

Karlsruhe Institute of Technology, Engesserstr. 7, 76131 Karlsruhe, Germany

[§]*Division of Chemistry and Chemical Engineering*

California Institute of Technology, Pasadena, California 91125, United States

[∥]*Department of Chemistry and Biochemistry*

University of California, Santa Barbara, California 93106, United States

[⊥]*California NanoSystems Institute and Institute of the Environment and Sustainability*

University of California, Los Angeles, CA 90095, USA

E-mail: avdv@ucsb.edu; seshadri@mrl.ucsb.edu

Abstract

Electrode materials for Li^+–ion batteries require optimization along several disparate axes related to cost, performance, and sustainability. One of the important performance axes is the ability to retain structural integrity though cycles of charge/discharge. Metal-metal bonding is a distinct feature of some refractory metal oxides that has been largely underutilized in electrochemical energy storage, but that could potentially impact structural integrity. Here $LiScMo_3O_8$, a compound containing triangular clusters of metal-metal bonded Mo atoms, is studied as a potential anode material in Li^+—ion batteries. Electrons inserted though lithiation are localized across rigid Mo_3 triangles (rather than on individual metal ions), resulting in minimal structural change as suggested by *operando* diffraction. The unusual chemical bonding allows this compound to be cycled with Mo atoms below a formally +4 valence state, resulting in an acceptable voltage regime that is appropriate for an anode material. Several characterization methods including potentiometric entropy measurements indicate two-phase regions, which are attributed through extensive first-principles modeling to Li^+ ordering. This study of $LiScMo_3O_8$ provides valuable insights for design principles for structural motifs that stably and reversibly permit Li^+ (de)insertion.

Introduction

Improving reversibility and lifetime of Li^+–ion electrode materials necessitates understanding structure-property relationships in electrode materials.[?] Increasing reliability and performance is imperative towards broader adoption of Li^+–ion battery-reliant technologies such as electric vehicles and portable electronics.[?][?] The poor cycle life of active materials in Li^+–ion batteries is often associated with structural degradation of the electrode.[?] The surface of a typical active material develops an interphase, that can evolve during cycling and contribute to irreversible Li^+ loss.[?] Particles fatigue over time from repeated expansion and contraction of the structure with lithiation and delithiation, respectively.[?] Repeated volume changes induce strain, causing particle cracking and lead to myriad issues, including contact and porosity loss, that negatively impact charge and ion transport.[?][?] The interphase degradation mechanism is significantly amplified with cracking since it additionally forms on all freshly exposed surfaces.[?] These serious failure mechanisms have motivated efforts to directly probe compositional and structural responses through scanning transmission electron microscopy[?] and strain measurements.[?] Even the promising Ni-rich layered cathode systems such as NMC811 suffer from degradation processes attributed to high interfacial lattice strain between the surface and bulk of the structure.[?]

Strategies to mitigate this type of failure mechanism vary widely, but all center around the principle of minimizing large volume changes during cycling. Engineering the electrode morphology has been shown to be successful at preventing lattice strain through using an intergrown rocksalt structure in a layered cathode.[?] Improved polymer binder design is also being explored.[?][?] Nanoscaling particles[?][?][?] and optimizing disorder[?] have been established as ways to suppress phase transitions and circumvent the innate volume expansion of certain crystal structures. Normally, delithiation of $LiCoO_2$ intrinsically causes a significant expansion of the c lattice parameter.[?][?] Judicious doping of certain materials, such as Al in $LiNi_{1-x}Al_xO_2$, is suggested to be effective at preventing large volume changes.[?]

3

Fast charging capabilities are highly desirable, but rapid Li^+ insertion can exacerbate particle cracking.[?] Efforts to improve ion transport include nano-structuring the active material through high energy ball milling or optimized synthetic routes to decrease Li^+ ion diffusion distances.[?][?][?] Carbon coating is used to improve electron transport between particles.[?] Although these approaches for both mitigating volume expansion and improving transport can be very effective, they mask the undesirable properties associated with the crystal structure itself. It is critical then to understand and identify crystallographic motifs on the atomic scale that intrinsically provide both good ion and electron transport pathways, while maintaining a rigid structural framework that prevents significant lattice expansion.

Crystallographic shear phases, including the Wadsley-Roth structures[?][?][?][?][?] possess crystallographic shear and have emerged as a promising and broad class of materials that display exemplary performance as electrodes. These materials are diverse in elemental constitution and block size, and even large particles of these materials are capable of impressive rates.[?][?][?][?][?][?][?][?][?][?] Computational and experimental efforts have suggested that a combination of corner and edge-sharing polyhedra promote metallic conductivity and fast Li^+–ion diffusion, while suppressing large structural changes.[?][?][?]

In this work we seek to explore other kinds of structural motifs that allow stable and reversible capacity retention. We turn to oxide compounds of Mo, the chemistry of which is varied and rich, in part because Mo is able to exist in a wide range of oxidation states, coordination geometry, and structural motifs.[?][?][?] Some of the first ternary oxides of Mo^{4+} were reported in 1957, with Mo–Mo bonding in triangular Mo_3 clusters and the formula $A_2^{II}Mo_3^{IV}O_8$, with the wide range of divalent cations Mg, Mn, Fe, Co, Ni, Zn, and Cd.[?] $LiScMo_3O_8$, the compound studied here, was discovered while exploring the possibility of using a monovalent and trivalent ion to replace two divalent cations.[?] Postulated site preferences based on cation charge and size in this series were confirmed from structural studies.[?][?] This $LiRMo_3O_8$ class of materials has garnered somewhat limited attention for

4

Li$^+$ insertion, with electrochemical studies on the structural analogues LiHoMo$_3$O$_8$[?] and LiYMo$_3$O$_8$.[?] The Chevrel phases M^{II}Mo$_6$S$_8$,[?] have in contrast, been extensively studied for Mg$^2+$,[?] Na$^+$,[?] and Li$^+$batteries.[?] Recent work on NaMoO$_2$ showed reversible Na intercalation.[?]

LiScMo$_3$O$_8$ serves as an effective model system for understanding and probing the effects of delocalized redox in Mo cluster compounds. Redox reactions are conventionally believed to proceed on individual atoms and ions, with some impact from the surrounding environment.[?] In contrast, the redox presented here occurs here on a cluster of atoms, that collectively create the molecular orbital states that are implicated. This has a number of important structural and electronic implications, with the MoO$_3$ clusters potentially serving as an electron reservoir. One of the many consequences is that the voltage range found for Li$^+$ insertion and de-insertion is more in line with a working voltage more appropriate for an anode than the higher voltages more typically associated with the Mo^{4+}/Mo^{6+} redox couple.[?]

The combination of experimental investigations and density functional theory (DFT) based calculations reveal the importance of Li$^+$ ordering in this system and its effect on the electrochemical properties. Stable and reversible cycling is demonstrated at rates up to 10 C. Minimal structural changes are observed in *operando* X-ray diffraction across the lithiation range employed. Evidence for phase coexistence regions are attributed to Li$^+$ ordering using potentiometric entropy measurements, as is also supported through extensive computational modeling including the enumeration of structural energetics with varying Li$^+$ content. Studies of battery materials in recent years has pointed to the need for better insights into the nature of bonding and the concept of oxidation state in battery materials.[? ? ? ?] Here we show that a deeper understanding of metal-metal bonding as an electronic and crystallographic motif could lead to materials with stable Li$^+$ cycling and minimal structural changes.

Results and discussion

Crystal and Electronic Structure
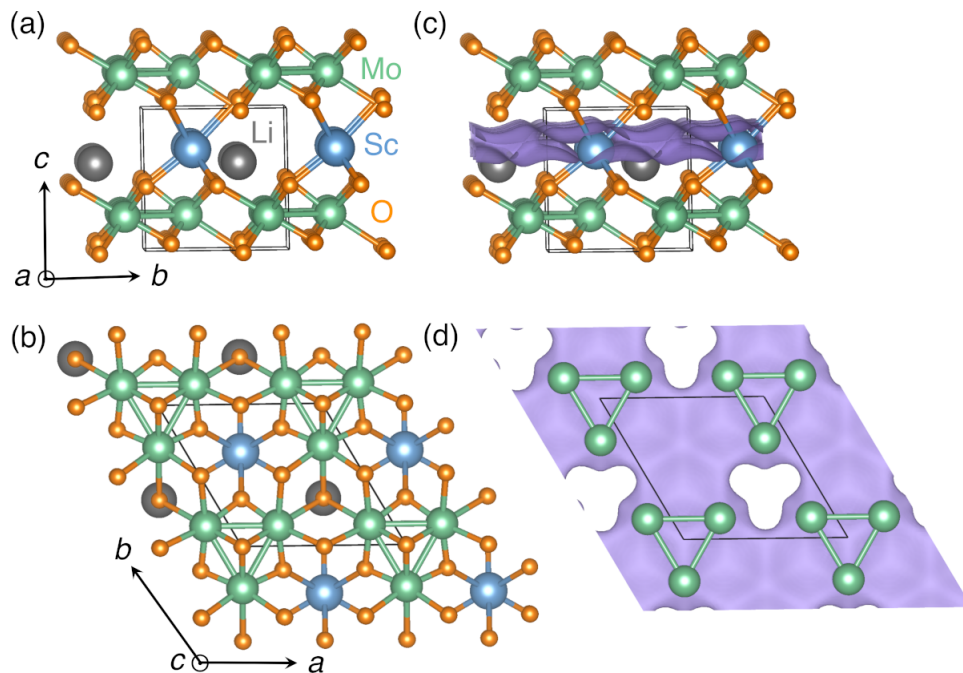

Figure 1: Crystal structure of $LiScMo_3O_8$ (space group is $P3m1$, No. 156) contains alternating layers of triangular clusters of metal-metal bonded Mo atoms and Li^+/Sc. Li^+ is tetrahedrally coordinated. (a) Side view and (b) top view of structure. (c, d) Side view and top view of the structure, respectively, with the bond valence difference map (purple isosurface) for Li^+ in the space of the structure displayed for an isosurface value $\Delta v = 0.2$ valence units.

Careful examination of the crystal structure of $LiScMo_3O_8$ is critical for understanding its electrochemical, structural, and electronic properties. The Mo cluster compounds get their namesake from a distinct structural motif, namely a kagomé lattice built of triangular clusters of metal-metal bonded Mo atoms. Figure 1(a) shows how this distinct motif is separated by an alternating layer of Li^+/Sc. In the Mo layer, MoO_6 octahedra form Mo_3O_{13} clusters that share some O between clusters. Although formally Mo^{4+}, Mo-Mo bonding accounts for the 6 d electrons in this electron precise structure. Traditional redox chemistry is typically considered on an individual atom. In this case, the metal-metal bonded Mo atoms provide a center for delocalized redox within the cluster, which is a much more

unconventional mechanism. We surmise that these clusters have a profound impact on the structural stability of the material with Li^+ insertion, and the overlapping d orbitals may have the potential to dampen volume expansion due to the delocalized nature of their electrons. Figure 1(b) gives the top down perspective along the c axis, illustrating how the Mo clusters are offset from the scandium atoms in the following layer. Each Mo is in a +4 oxidation state, sharing one electron with each neighboring Mo atom. Because of the lower starting oxidation state of Mo, we will not be able to access multielectron redox. This instead will provide a platform for a good anode potential using the Mo^{4+} to Mo^{3+} redox couple, in sharp contrast to other Mo-based oxides such as MoO_3 that fall in between conventional anode and cathode voltages.[?]

Bond-valence sum mapping is a useful tool to approximate ion transport pathways within a 3D crystal structure. The valence difference (Δv) between the probe ion, in this case Li^+, and the actual electrostatic valence, can be roughly related to the activation energy required for ion transport. Therefore, mapping the valence difference provides a means of visualizing possible Li^+ migration paths.[?] The isosurface for a $\Delta v = 0.2$ in valence units for $LiScMo_3O_8$ is shown in panel (c) and (d) of Figure 1. This isosurface illustrates a probable ion conduction region within the Li^+/Sc layer, suggesting low energy 2D diffusion. Unsurprisingly, the isosurface also indicates that there is no expected ion conduction through the metal-metal bonded Mo layers.

To understand the electronic structure of $LiScMo_3O_8$, density-functional theory-based structure calculations are utilized to provide qualitative insight about this material as a Li^+ host. The density of states, displayed in Figure 2, shows filled Mo d-states just below the Fermi level and a large band gap, indicating the starting material is an insulator. Any additional electrons would begin to fill the Mo d-states around 2 eV. However, these states are very localized and the small dispersion indicates that even with Li^+ insertion, this material would not become a good conductor. Additionally, the large gap in the DOS between filled and unfilled states foreshadows a potential two-phase reaction. The higher energy states
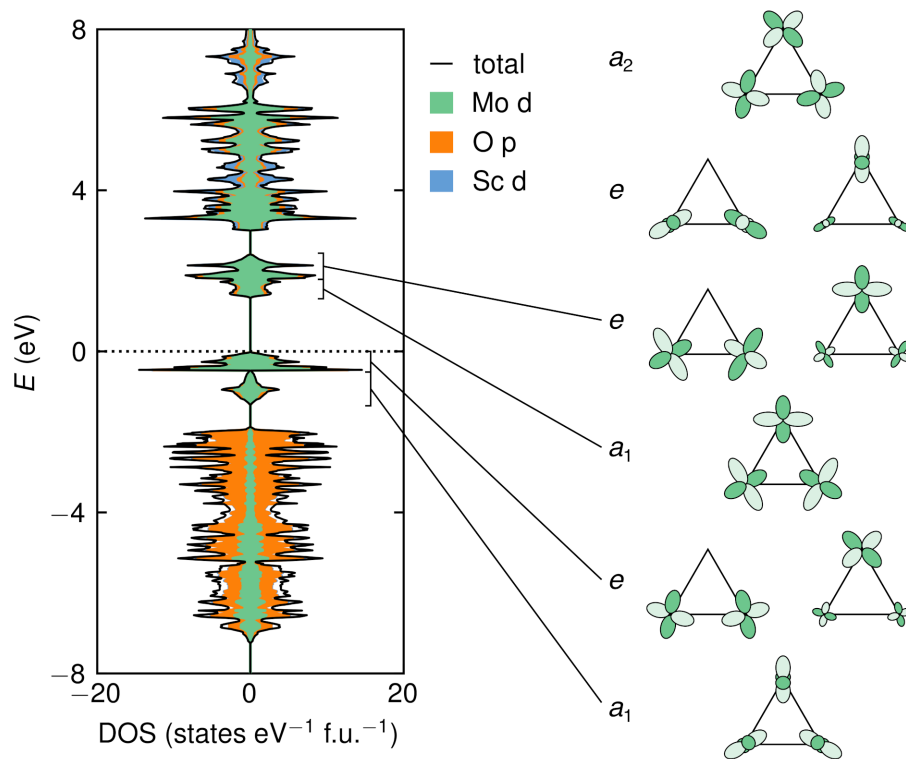
7

Figure 2: Spin-polarized density of states of LiScMo$_3$O$_8$ alongside the molecular orbitals formed by the Mo t_{2g} orbitals. Molecular orbitals are ranked by energy in the order determined by Tsuge *et al.*[?]

will not be able to continuously fill and therefore inserting Li^+ could thermodynamically favor a lower energy phase. The majority of states near the Fermi level comprise of Mo d-states.

A molecular orbital (MO) diagram can help to understand the nature of the Mo bonding in the context of the electronic structure more specifically. A qualitative MO diagram was worked out for equilateral Mo_3 triangles by Tsuge *et al.*[?] Figure 2 shows an adapted version of their proposed MO diagram, and how each specific energy level corresponds to the DOS. The six electrons for each cluster occupy the three bonding MOs. If there are more electrons, these occupy the upper a_1 or e MOs that arise from more weakly interacting AOs. The metal d-orbitals of the clusters play an important role with Li^+ insertion. As more electrons are inserted, they will occupy higher energy MOs.
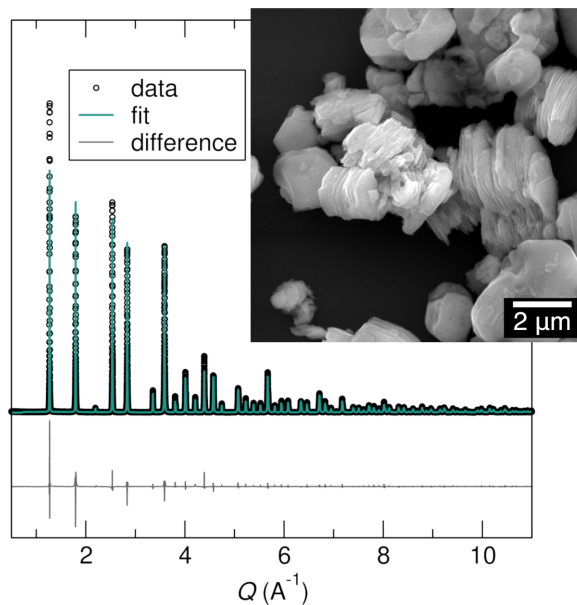

Figure 3: 11-BM synchrotron powder X-ray diffraction data for $LiScMo_3O_8$ shows a single phase of the target layered structure. Refinement statistics can be found in Table S1 in the Supporting Information. The inset displays a scanning electron micrograph of $LiScMo_3O_8$ crystallites with plate-like structure.

Prior studies indicated some difficulty in obtaining a phase pure material.[?] Optimization of precursor powders, in conjunction with a purification step, allowed us to realize a phase-pure sample as a black powder. This structure was characterized with powder

9

synchrotron X-ray diffraction, as shown in Figure 3. Refinement statistics are shown in Table S1 in the Supporting Information. Future work will use neutron diffraction to develop a more complete picture of the structure. Characterization of this material using electron microscopy reveals important insights at multiple length scales. SEM on the bulk powder particles shows micron-sized particles that are comprised of highly crystalline sheets stacked on top of each other. The anisotropic morphology of these particles allows for access to Li^+ along the edges of the sheets, but not through the faces.

Looking more closely at the crystalline sheets in Figure 4(a), using aberration-corrected high resolution transmission electron microscopy, we see how these thin sheets layer along the edge of a particle. We additionally use this technique to directly observe the atomic lattice along the [001] plane.[Figure 4(b)] The resulting image resolves the expected hexagonal tiling characteristic of the kagomé-structured Mo sheets. The inset simulation using our model structure blends seamlessly with experiment.

Electrochemistry

We first aim to understand the charge storage properties of this material through a variety of electrochemical cycling experiments displayed in Figure 5. Figure 5(a) shows variable rate galvanostatic cycling. At the slowest rate, as Li^+ intercalates into $LiScMo_3O_8$, a large, flat plateau occurs at 1.5 V. This plateau region extends as nearly an additional 1.25 Li^+ are inserted and the stoichiometry is $Li_{2.25}ScMo_3O_8$. A more subtle plateau occurs immediately after, followed by a relatively smooth sloping regime until maximum lithiation. This material is capable of storing an additional 2 Li^+ at slow rates, for a capacity close to 120 mAh g^{-1}. Upon charging, the material displays no polarization for the matching short and long plateau at 1.5 V, but notably contains an additional unsymmetrical plateau slightly above 2 V. As the cycling rate is increased, the length of the plateau gradually diminishes up to a 10C rate. Although $LiScMo_3O_8$ does not store a significant amount of charge at fast rates, we show as a proof of concept that it is capable of cycling quickly and that the
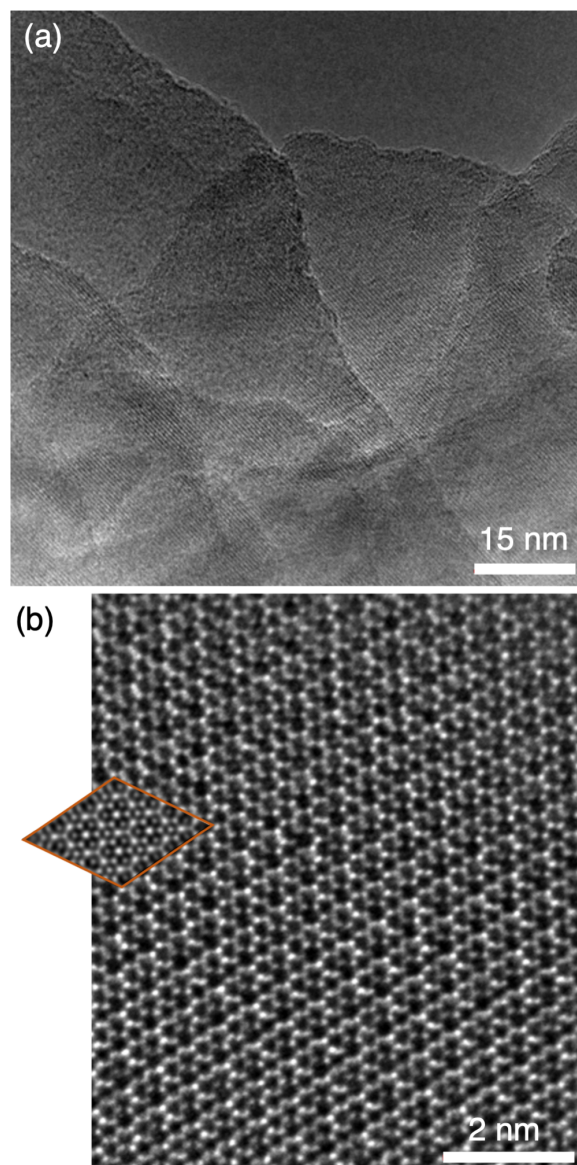
10

Figure 4: (a) Aberration-corrected high resolution transmission electron microscopy (HRTEM) shows how the thin, crystalline sheets overlap along the edge of a powder particle. (b) HRTEM also shows highly ordered hexagonal tiling characteristic of a kagomé-type network. The orange inset contains a HRTEM simulation of three stacked unit cells of $LiScMo_3O_8$ along the [001] direction. The simulation parameters include an energy of $300\,keV$, a defocus spread of 3 nm, a C_s of $+2\,\mu m$, and a slice thickness of $0.1\,nm$.
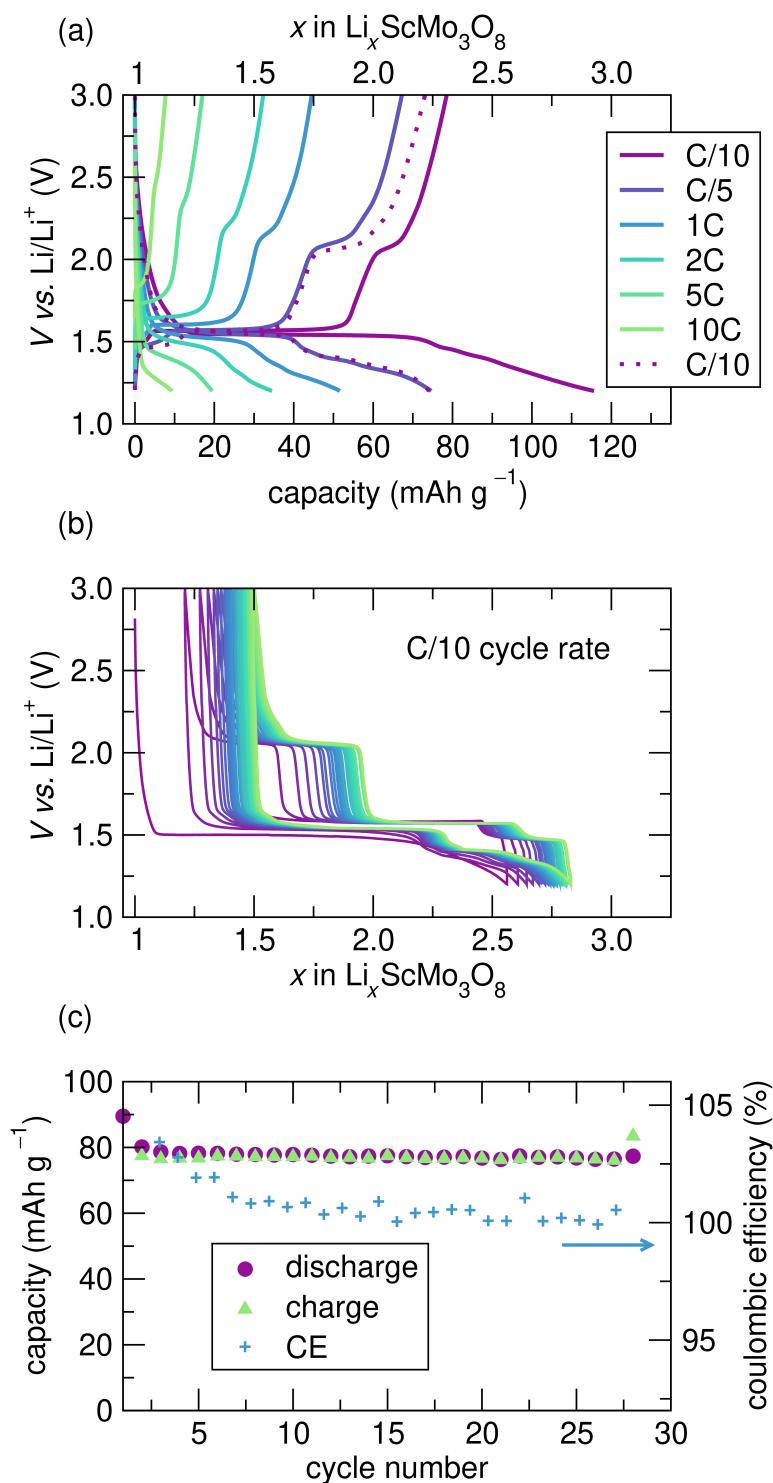
Figure 5: Electrochemistry of LiScMo$_3$O$_8$. (a) Galvanostatic cycling at rates from C/10 to 10C and its recovery. (b) Galvanostatic cycling at a C/10 rate shows slight irreversible capacity loss after the first cycle but highly reversible features. (c) summarizes the rate retention capability of LiScMo$_3$O$_8$ from the galvanostatic cycling in figure(b).

material is able to recover again at slow rates. Because Li^+ can only diffuse through the edges of these micron-sized sheets, it is possible that the particle morphology is limiting the capacity retention at fast rates. While outside of the scope of this fundamental study, it is proposed here that the rate capability could be greatly increased with morphology optimization.

Extended cycling of $LiScMo_3O_8$ shows highly repeatable and reversible features in the voltage curve. Figure 5(b) overlays the discharge curves at a C/10 rate over 30 consecutive cycles. After the first cycle, there is clearly some initial capacity loss, but the major features, notably the plateaus, remain highly reproducible with no changes to the voltage. Figure 5(c) summarizes the extended cycling, highlighting its stable capacity retention. The coulombic efficiency hovers around 100%. The initial points over that threshold are possibly due to some small side reaction, but this does not significantly affect the reversibility or capacity. Electrochemical impedance spectra of slurry electrodes as a function of Li^+ content indicate that the charge transfer resistance remains constant over the lithiation range investigated, consistent with the calculated electronic structure of the starting material. (Figure S1 in the Supporting Information)

As Li^+ inserts into the structure, delocalized redox on the Mo clusters should result in a reduction of the Mo oxidation state. Following the equation $LiScMo_3O_8 + x\,Li^+ + x\,e^{-1} \rightarrow Li_{1+x}ScMo_3O_8$ the theoretical capacity would be 172 mAh g^{-1} if 3 e$^-$ per formula unit are inserted ($x = 3$), where we assume each Mo^{4+} reduces to Mo^{3+}. We probe this expected change in chemical bonding through *ex situ* X-ray photoelectron spectroscopy (XPS). Although experimentally only 2 e$^-$ per formula unit are inserted, we are able to both qualitatively and quantitatively observe a marked evolution of the Mo chemical bonding environment. Figure 6 (a) shows the spectrum of the pristine material, where all Mo atoms are in the expected $+4$ oxidation state, showcasing the characteristic doublet of the d orbital. After insertion of 1.84 Li^+, Figure 6 (b) displays the drastic change in spectrum with the emergence of an additional doublet at lower binding energy, signifying coexistence of both
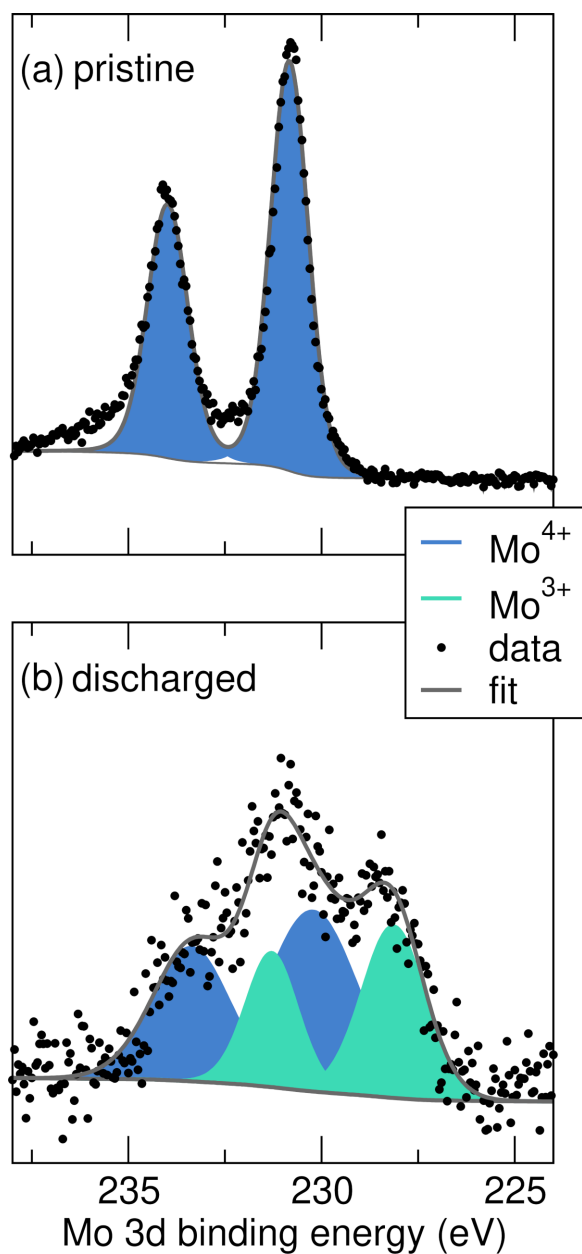
Figure 6: X-ray photoelectron spectra displaying the Mo 3d binding energy region for (a) pristine $LiScMo_3O_8$ and (b) discharged material ($Li_{2.84}ScMo_3O_8$). The pristine material contains only Mo^{4+} while the discharged material contains both Mo^{3+} and Mo^{4+}. The binding energy of the Mo^{4+} peaks do not match precisely, due to the unusual metal-metal bonding feature in the structure.

Mo^{4+} and Mo^{3+} states. This sample was discharged to $Li_{2.84}ScMo_3O_8$, therefore we would expect 62% of the Mo atoms to be Mo^{3+} by balancing the oxidation states. Experimentally we measure this value to be 41% through quantification in CasaXPS software. These values could deviate due to a combination of surface sensitivity to oxidation and more importantly, complexity arising due to the presence of metallic states. It is notable that the clusters allow reduction to the Mo^{3+} oxidation state, resulting in a lower working voltage than the Mo^{6+}/Mo^{4+} couple.
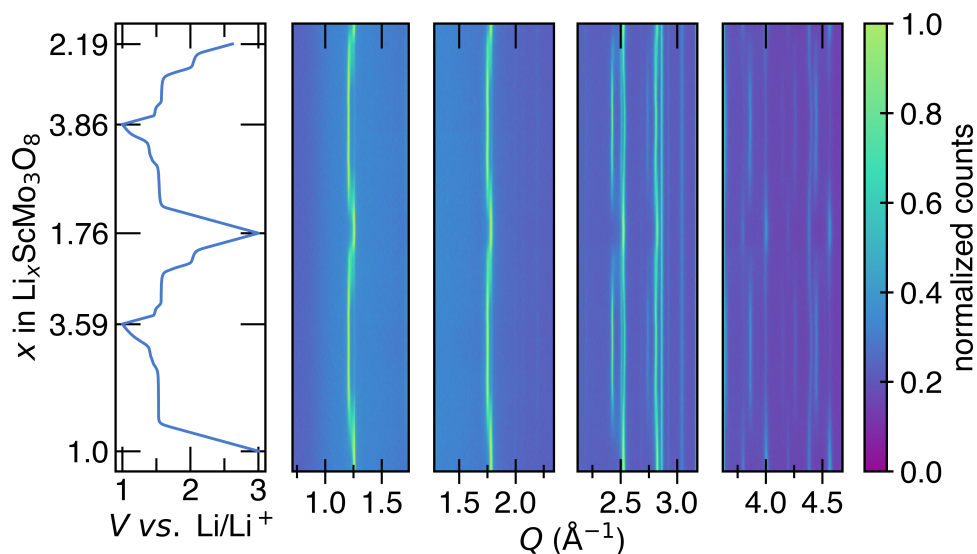
Figure 7: *Operando* X-ray diffraction of $LiScMo_3O_8$ during the first two galvanostatic discharge/charge cycles at a C/15 cycling rate. The electrochemistry is shown in the left-most panel, inserting over two additional Li^+ to $Li_{3.59}ScMo_3O_8$ on the first discharge. Select regions of the diffraction patterns are shown as a heat map to better visualize the evolution of the diffraction peaks.

The structure of a voltage curve gives direct insight into chemical changes of a system. There is a relation between the Gibbs free energy and voltage curve, so phase transformations will have clear signatures in the profile, manifesting as a plateau.[?] Because the electrochemistry of this system shows such clear plateaus, we expect there to be phase transitions. *Operando* X-ray diffraction is used to understand the evolution of the structure with lithiation. Figure 7 shows a heat map of select panels highlighting the major diffraction peaks as over 2 additional Li^+ are slowly inserted. We observe subtle changes

and shifts to these peaks, consistent with a two-phase reaction. The full data range can be found in Figure S2 and Figure S3 in the Supporting Information. Most layered electrode materials exhibit greater signs of expansion, but the *operando* diffraction data show only slight strain in the structure.

A series of X-ray diffraction spectra were extracted from the *operando* data set to allow for comparison between the experimental and simulated diffraction patterns. Figure 8 shows select panels comparing the experimental and simulated diffraction patterns as function of lithiation. We see slight shifts and the emergence of new peaks, consistent with a two-phase reaction. There is good agreement between experiment and simulation, and the emergence of new peaks is captured well by the calculations. The full simulated Q range can be found in Figure S6 in the Supporting Information. Figure 8(e) compares experimentally observed unit cell volumes to calculated volumes of predicted ground state structures from DFT. These extensive calculations are discussed in detail in the following section. Going from $LiScMo_3O_8$ to $Li_3ScMo_3O_8$, calculations predict a small volume expansion of 2%, which is comparable to the typical prediction error for bulk solids of the DFT functional used (SCAN).[?][?] The *operando* and experiments shows 3% change in volume with lithiation, in line with calculations predicting minimal perturbation to the structure.

From a structural standpoint, X-ray diffraction does not show any major changes with Li^+ insertion, but XPS concludes that Mo is being reduced on the clusters. Raman spectroscopy allows us to probe the vibrational modes in crystal structures associated with bonding. We use *operando* Raman spectroscopy to better understand what changes are happening to the crystal structure of $LiScMo_3O_8$, since the changes are subtle and dominated by bonding of the Mo clusters. Figure 9 shows Raman spectra as a function of Li^+ content during discharge and charge. A smaller amount of Li^+ was inserted than desired due to non-optimized electrochemistry in the custom *operando* cell. (Figure S5 in the Supporting Information) Despite this, we are still able to gain important insight about the changes to the Mo bonding with lithiation.
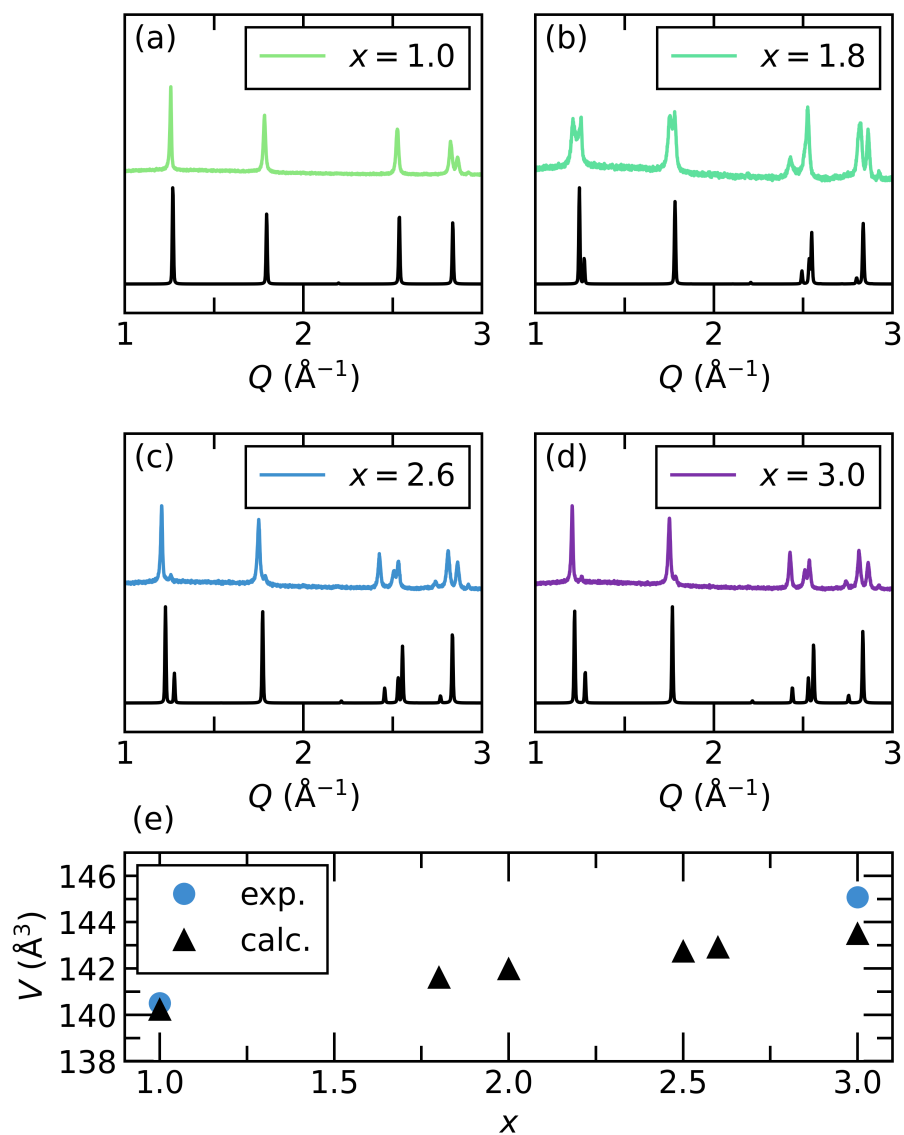
Figure 8: Select panels comparing the extracted X-ray diffraction pattern for $Li_xScMo_3O_8$ from the *operando* experiment and the DFT simulated diffraction pattern below for corresponding lithiation values (a) $x = 1.0$ (b) $x = 1.8$ (c) $x = 2.6$ and (d) $x = 3.0$. There is relatively good agreement between the experimental and simulated diffraction. (e) Comparison of the calculated volumes of lowest energy structures determined from DFT, and experimentally measured unit cell volumes from *operando* lab diffraction. DFT predicts low volume expansion, which is confirmed with the data set showing a volume expansion of 3%.
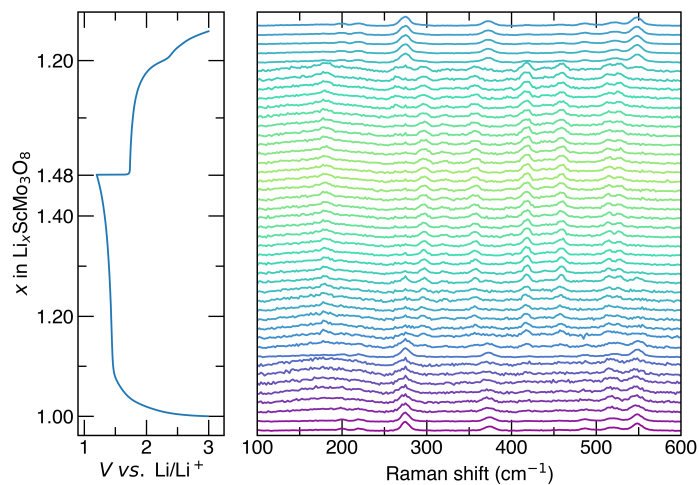
Figure 9: *Operando* Raman spectroscopy of $LiScMo_3O_8$ during the first galvanostatic cycle at a C/20 cycle rate. The corresponding electrochemistry is shown in the left panel, where 0.48 Li^+ are inserted to form $Li_{1.48}ScMo_3O_8$.
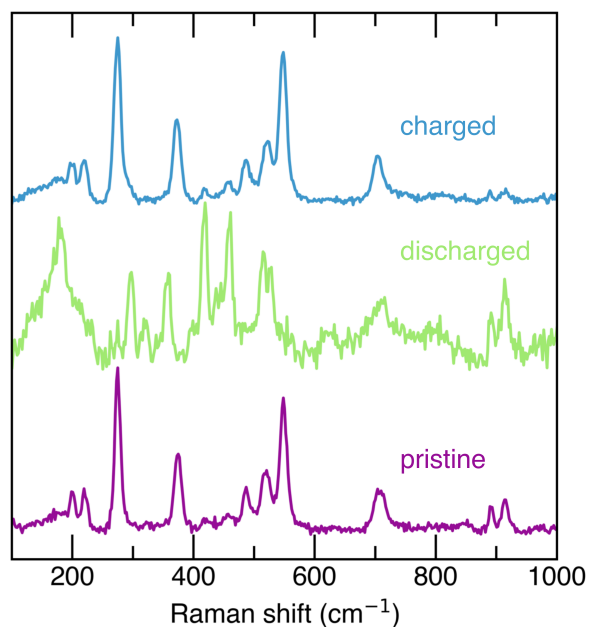

Figure 10: Select *operando* Raman spectroscopy spectra from Figure 9, displaying the pristine spectrum, the fully discharged spectrum, and the fully charged spectrum. The similarity between the pristine and fully charged spectra indicate the reversibility of the Raman modes.

18

The initial spectrum measured in *operando* matches well with the *ex situ* spectrum measured *ex situ* (Figure S6 in the Supporting Information), which confirms that the modes are related to the active material. Although it is difficult to accurately assign Raman modes, we use literature on similar systems containing Mo clusters to interpret the data. Literature indicates that the $370\,\mathrm{cm}^{-1}$ mode corresponds to a Mo cluster breathing mode.[?][?][?][?] After 0.1 Li$^+$ inserts, this peak shifts to lower wavenumbers. In the context of the MO diagram (Figure 2), as Li$^+$ inserts, electrons begin to fill a higher energy antibonding orbital of the Mo cluster. This would weaken the Mo-Mo bonds and result in a softer stretch, which is observed experimentally. As the cell is charged and Li$^+$ is removed, the same peak abruptly shifts back to the original position. Adding Li$^+$ changes the local symmetry of the material, resulting in different allowed and forbidden Raman modes. However, we observe similar modes between $LiScMo_3O_8$ and $LiZn_2Mo_3O_8$, allowing the modes associated with the Mo_3O_{13} molecular units to be identified.[?] And although we cannot assign all the new modes, they do revert back to those observed in the pristine spectra. An expanded comparison of the pristine, discharged, and charged spectra in Figure 10 underscore the highly reversible nature of the Mo_3 breathing mode and experimentally indicate the structural importance of the Mo clusters and their d-orbital overlap for Li$^+$ insertion.

Entropic potential measurements and Li$^+$ ordering

This material shows clear plateaus in the electrochemistry, indicating phase coexistence. Diffraction experiments indicate slight evolution of the crystal structure, consistent with two-phase regions. To better understand the nature of the phase coexistence, we combine insights from experimentally obtained entropic potential measurements and extensive DFT-based calculations, conclusively determining that Li$^+$ ordering drives these features. Figures 11(a) and 11(b) plot the open circuit voltage $U_{ocv}(x, T)$ and the operating voltage $V(x, T)$ during lithiation and delithiation, respectively. GITT consists of applying constant current pulses, followed by a relaxation period at $20\,^\circ\mathrm{C}$ to allow the system to reach
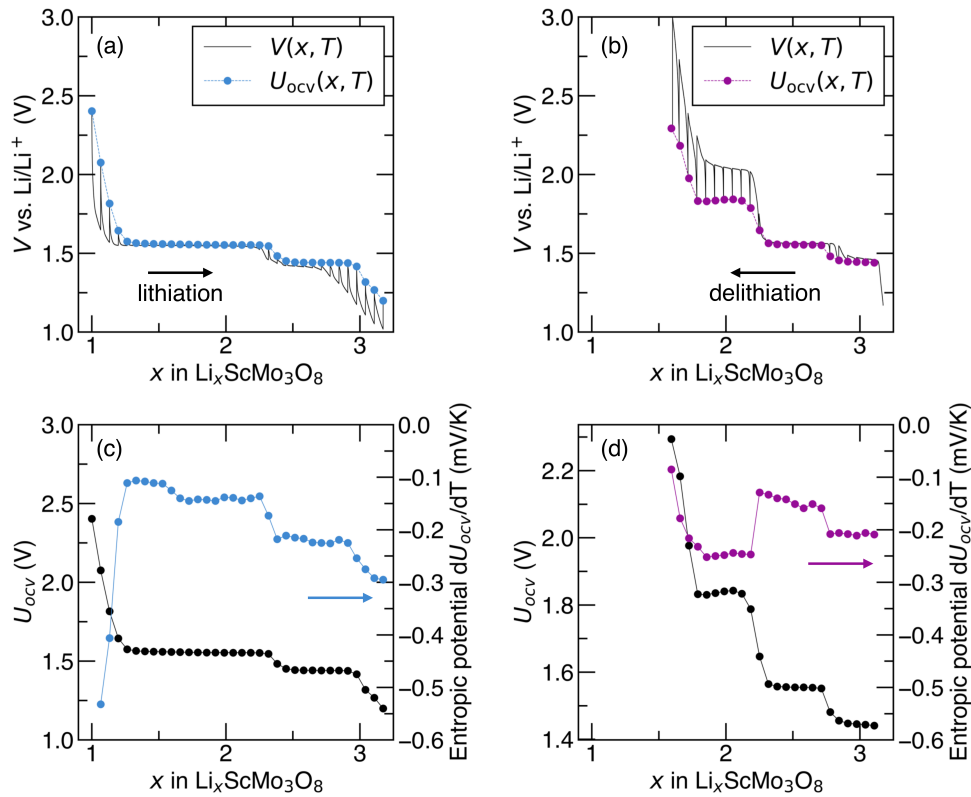
Figure 11: Open circuit voltage $U_{ocv}(x, T)$ and operating voltage $V(x, T)$ during (a) lithiation, (b) delithiation, and $U_{ocv}(x, T)$ and entropic potential $\partial U_{ocv}(x, T)/\partial T$ during (c) lithiation, (d) delithiation as functions of Li^+ composition x in $Li_x ScMo_3 O_8$ at a rate of C/10 and at 20 °C.

equilibrium, allowing observation of the dynamic behavior of $V(x, T)$ and measurement of thermodynamic properties such as $U_{ocv}(x, T)$. During lithiation, the $U_{ocv}(x, T)$ curve clearly shows two plateaus, corresponding to two separate phase coexistence regions. The overpotential, defined as $[V(x, T) - U_{ocv}(x, T)]$, was much smaller in the first voltage plateau at 1.6 V compared to the second voltage plateau at 1.4 V, suggesting relatively fast kinetics of Li$^+$ intercalation in the former.[?] Disparate from lithiation, $U_{ocv}(x, T)$ the delithiation process features three voltage plateaus at 1.8 V, 1.6 V, and 1.4 V [Figure 11(a)]. Once again though, the overpotential in the voltage plateau at 1.6 V was much smaller than that in the voltage plateaus at 1.8 V and 1.4 V, again indicating relatively fast kinetics of Li$^+$ deintercalation at that voltage.

Figure 11(c) plots the open circuit voltage $U_{ocv}(x, T)$ and the entropic potential $\partial U_{ocv}(x, T)/\partial T$ at 20 °C as functions of x in Li$_x$ScMo$_3$O$_8$ at a rate of C/10 during lithiation. At the beginning of lithiation, for $x \leq 1.25$, both $U_{ocv}(x, T)$ and $\partial U_{ocv}(x, T)/\partial T$ exhibit smooth sloping curves, indicating Li$^+$ intercalation in a homogeneous solid solution.[?] For $1.25 \leq x \leq 2.25$, $U_{ocv}(x, T)$ was constant at 1.6 V, suggesting two-phase coexistence. However, $\partial U_{ocv}(x, T)/\partial T$ measurements show two distinct plateaus in the same region. Therefore, it is likely that there are two instances of phase coexistence in the regions 1.25 $\leq x \leq 1.6$ and $1.6 \leq x \leq 2.25$. $\partial U_{ocv}(x, T)/\partial T$ was slightly larger for for the first region than the second one, suggesting a transition to a more ordered structure. Both $U_{ocv}(x, T)$ and $\partial U_{ocv}(x, T)/\partial T$ for $2.25 \leq x \leq 2$ were constant and independent of x, confirming a single two-phase coexistence region. After $x \geq 3$, both $U_{ocv}(x, T)$ and $\partial U_{ocv}(x, T)/\partial T$ are sloping curves corresponding to lithiation in a homogeneous solid solution.

We similarly analyze $U_{ocv}(x, T)$ and $\partial U_{ocv}(x, T)/\partial T$ during delithiation (Figure 11(d)). At the beginning of delithiation, for $3.2 \geq x \geq 2.25$, both $U_{ocv}(x, T)$ and $\partial U_{ocv}(x, T)/\partial T$ feature two plateaus, analogous to those observed during lithiation and identical in magnitude. This is an indicator of structural reversibility. At the end of delithiation ($2.25 \geq x \geq 1.6$), $U_{ocv}(x, T)$ contains another plateau at 1.8 V. Here, the measured $\partial U_{ocv}(x, T)/\partial T$ is

21

smaller than that at 1.6 V during lithiation. The smaller $\partial U_{ocv}(x,T)/\partial T$ indicates a smaller partial molar entropy, suggesting the transition on delithiation is more ordered than that at the same voltage on lithation. Entropic potential measurements enhance our understanding of phase coexistence in this system, while DFT is used to ascertain the more fine mechanistic details.

DFT calculations were performed to explore Li$^+$ ordering preferences with varying composition x in Li$_x$ScMo$_3$O$_8$. The calculated formation energies of many distinct Li$^+$-ordered configurations and the resulting voltage profile are shown in Figure 12, with the relaxed structures of select predicted ground state configurations shown in Figure 13. At $x = 1$, the synthesized LiScMo$_3$O$_8$ structure shown in Figures 1 and 13(a) is predicted to be stable. In this structure, the Li$^+$ exclusively occupy one of the two tetrahedral sites that do not share faces with Sc sites. The other such tetrahedral site lies directly above/below the centers of the Mo$_3$ clusters, rather than between them, and as a result is much less favorable for Li$^+$ occupation (1.05 eV per formula unit higher in energy at $x = 1$). At $x = 3$, the other composition extreme, all the octahedral Li$^+$ sites are filled, as shown in Figure 13(b). For $1 < x < 3$, the low-energy configurations display a mix of tetrahedral and octahedral Li$^+$, as indicated by the colors in Figure 12(a). Simulated X-ray diffraction patterns for selected ground state structures are shown in Figure S6 in the Supporting Information. Small deviations in relative intensity and peak positions between the simulated and experimental diffraction patterns are attributed to the perfect ordering associated with DFT cells that are not representative of the actual experimental system.

Although all calculations were initialized with ferromagnetic (FM) moments, some configurations spontaneously relaxed to non-FM configurations of the Mo$_3$ cluster moments. Additionally, for the predicted FM ground state structure at $x = 2$ (Figure 13(c)), we recalculated its energy with an antiferromagnetic (AFM) ordering of the two distinct Mo$_3$ cluster moments, which lowered the energy by 10 meV per formula unit. This preference for AFM ordering is consistent with the reported magnetic behavior of the related material
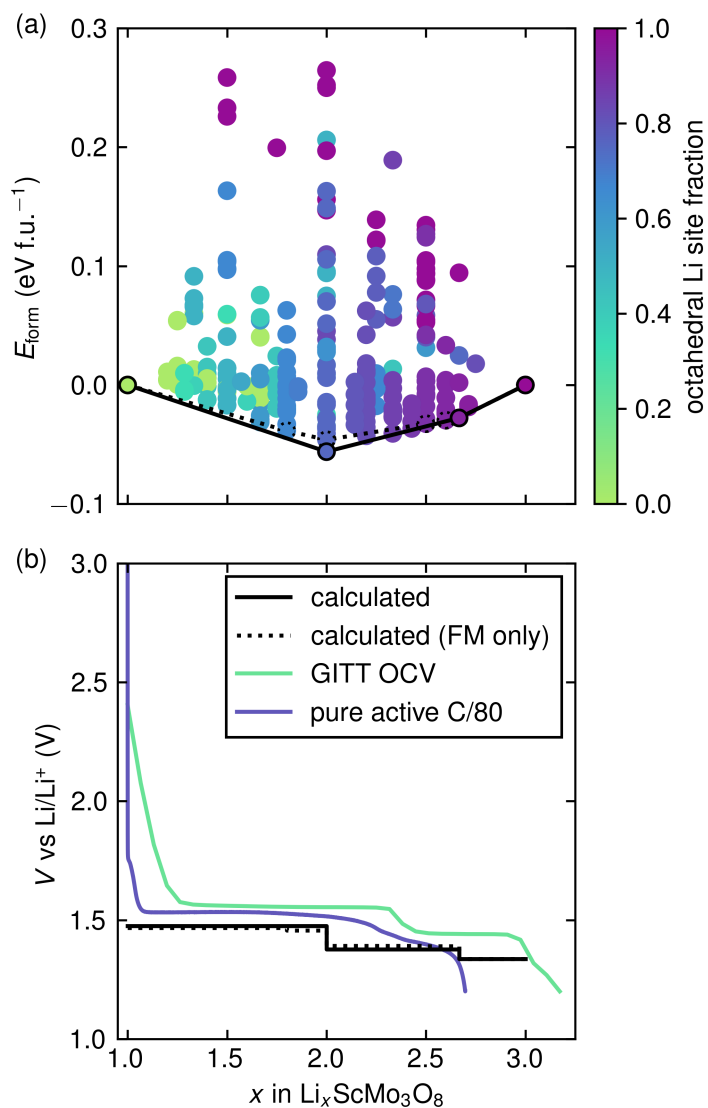
Figure 12: (a) Calculated formation energies of distinct Li$^+$-vacancy orderings in Li$_x$ScMo$_3$O$_8$. Points are colored by the fraction of Li$^+$ in the structure that occupy octahedral sites (as opposed to tetrahedral sites). The solid black line is the convex hull of all calculated configurations, while the dotted black line is the convex hull of only those configurations that retained a ferromagnetic state. (b) Calculated equilibrium voltage profiles for all configurations (solid black line) and ferromagnetic configurations only (dotted black line). Two different experimental voltage profiles from lithiation are also shown.
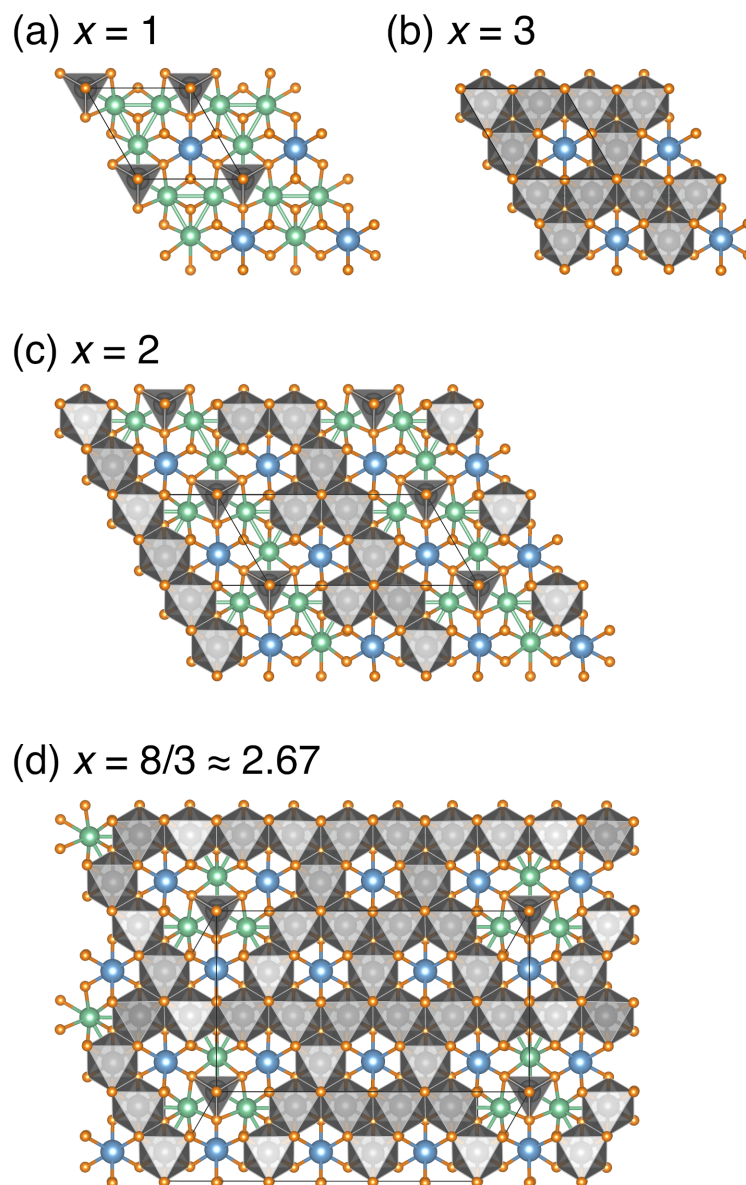
Figure 13: Relaxed structures of the calculated Li$^+$-vacancy-ordered ground state configurations in Li$_x$ScMo$_3$O$_8$ at (a) $x = 1$, (b) $x = 3$, (c) $x = 2$, and (d) $x = 8/3$. Coordination polyhedra are shown for Li$^+$ only. Structures visualized using VESTA.[?]

Li$_2$ScMo$_3$O$_8$.[?] However, as illustrated in Figure 12(b), including the non-FM configurations does not significantly alter the predicted voltage. The predicted voltage is overlaid with two experimental voltage curves, one from GITT (cast electrode) in Figure 11(a), and one from a pure active cell discharged very slowly. Both experimental voltages are in extremely good agreement with the calculated voltage. The second plateau of the pure active cell is slightly smoothed out, but the GITT curve captures both distinct plateaus. The apparent deviation in composition between the calculated and GITT voltage curves could indicate a slight overestimate of x in the experiment or the existence of an additional ground state ordering above $x = 2$.

Examining the predicted ground state structures (Figure 13) reveals a common Li$^+$ ordering motif among them. Essentially, the low-energy structures between $x = 1$ and $x = 3$ seem to interpolate those endpoint orderings, with some Li$^+$ occupying tetrahedral sites and the rest occupying the octahedral sites that do not share faces with the occupied tetrahedral sites. This always leaves three vacant octahedral sites around each occupied tetrahedral site. The tetrahedral Li$^+$ can be situated in various ways, such as rows [Figure 13(c)] or more isolated arrangements [Figure 13(d)]. As shown in Figure S7 of the Supporting Information, configurations that follow this Li$^+$ ordering motif generally lie lower in energy than those that do not. While we calculated all such motif-based configurations in supercells up to five times the volume of the primitive cell volume, it is quite possible that there are additional stable Li$^+$ orderings following this pattern in larger supercells. The entropic potential determined from calorimetry clearly shows phase coexistence regions. These DFT calculations explicitly attribute the phase coexistence to Li$^+$ ordering and filling motifs that give rise to two distinct voltage plateaus in electrochemistry, closely matching experimental results.

25

Conclusion

LiScMo$_3$O$_8$ serves as an effective model system for examining the possibility that metal-metal bonding can be used as a design principle for electrode materials. Electrochemical studies show highly reversible and stable cycling in a voltage range that is appropriate for use in Li$^+$–ion batteries. *Operando* X-ray experiments suggest minimal strain in the crystal structure with lithiation, pointing to the rigidity of the structure arising from metal-metal bonding between Mo. Diffraction also reveals a two-phase region expected from the voltage profile. Raman spectroscopy clearly show lowering of symmetry that would also correspond to a phase change, and softening of vibrational modes associated with the triangular Mo$_3$ clusters. Potentiometric entropy measurements explicitly show phase coexistence regions. The calculated voltage curve shows close agreement to experimental electrochemistry and provides powerful insight at the atomic level. Notably, detailed electronic structure calculations suggest that phase coexistence is associated with Li$^+$ ordering, as is also supported by the entropic potential measurements. The Mo$_3$ clusters in LiScMo$_3$O$_8$ effectively minimize structural changes because of the distributed charge. Understanding this unusual electrode material inspires the search for related materials for stable, low-strain electrodes.

Methods

Preparation of LiScMo$_3$O$_8$ LiScMo$_3$O$_8$ was prepared through a two-step synthesis process first involving conventional solid state calcination, followed by purification using a dilute acid wash. The starting materials were Sc$_2$O$_3$(Sigma Aldrich, 99.995%), Li$_2$MoO$_4$(Sigma Aldrich, 99.9%), Mo (Sigma Aldrich, 100 mesh, 99.9%), and MoO$_2$ (Sigma Aldrich, 99%). Li$_2$MoO$_4$ was dried overnight at 120 °C, Mo was heated overnight at 900 °C in 5% H$_5$/Ar, and MoO$_2$ was heated overnight at 400 °C in 5% H$_5$/Ar. The preparation steps for the precursor powders are key to ensuring purity by removal of water in the case of the salt Li$_2$MoO$_4$, and correct oxidation states in the case of the Mo and MoO$_2$. The cleaned starting materials were ground together in the exact molar ratio in an agate mortar for 20 minutes. The mixed powder was pressed into a 600 mg pellet, placed into an alumina crucible, and sealed in a silica tube that was back-filled with a partial pressure of Ar. The tube was heated at 790 °C for 24 hours, and water-quenched to room temperature. The reacted pellet was ground to a fine powder and washed in a 2 M HNO$_3$ solution with a 2 hour soak time. The acid wash was necessary to remove trace amounts of residual MoO$_2$. The powder was then washed three times with deionized water to remove any remaining acid traces. The washed powder was then heated gently in a vacuum oven to evaporate residual water. The purified material was stored under inert atmosphere. To confirm sample purity, powder diffraction data were collected at the high-resolution beamline 11-BM at the Advanced Photon Source at Argonne National Laboratory ($\lambda = 0.458118$ Å). Rietveld refinements to the previously published structure[?] were performed using TOPAS Academic v.6.[?] All visualization involving crystal structures was carried out using VESTA.[?]

Microscopy   A powder sample of LiScMo$_3$O$_8$ was dispersed in ultrapure water and subjected to an ultrasonic bath for 5 min to separate the particles. The suspension was then either drop-cast on a Si wafer for SEM investigation or nebulized by an ultrasonic evaporator onto a TEM grid with an ultrathin carbon support film. SEM investigation was carried

out using a FEI Quanta SEM, operated at 20 kV. TEM data was acquired with an image-side aberration corrected FEI Titan with CEOS corrector, operated at a primary energy of 300 keV. The spherical aberration was tuned to be 2 μm and images were acquired using a 4k CMOS camera (TVIPS XF416) in suitable zone axes. Data were analyzed with GMS 3 and imageJ.

Electrochemistry Electrochemial studies were performed on composite films cast on copper foil in an 80:10:10 (wt-%) ratio of active material:conductive carbon(TIMCAL Super P): polyvinylidene fluoride (PVDF). The active material and carbon were ball milled together in a small canister for 30 minutes, and then combined with PVDF dissolved in NMP to form a slurry. The mixture was mixed in a FlackTek speed mixer at 2000 rpm for 30 minutes. The slurry was cast using a 120 μ doctor blade and dried in a vacuum oven at 100 °C. The electrodes were punched into 10 mm diameter disks with a loading between 1 mg cm^{-2} to 2 mg cm^{-2}. Swagelok cells were used for electrochemical testing and were fabricated in an Ar-filled glovebox with 1 M LiPF$_6$ in EC/DMC 50/50 v/v (Sigma Aldrich) with a polished Li foil counter electrode and glass fiber separator (Whatman GF/D). Cells were discharged to 1.2 V and charged to 3.0 V using BioLogic potentiostats VMP1 and VMP3. One additional Li$^+$ per formula unit was assumed to insert into the crystal structure for calculating C rates.

Operando **X-ray diffraction** *Operando* X-ray diffraction was collected using a custom Swagelok-type cell with a Be window approximately 120 μm thick, allowing X-ray penetration into the cell while cycling. X-ray diffraction data were collected using a laboratory-source Panalytical Empyrean diffractometer with Cu-Kα radiation in Bragg-Brentano geometry. The same Li foil counter electrode, electrolyte, and composite ratio [80:10:10 (wt-%) active:SuperP:PVDF] were used as previously described. The only exception was that the slurry was cast to a slightly thicker 150 μm layer, directly onto Celgard separator, to improve diffraction counts. The cast electrode was placed face down onto the Be win-

dow, and a Whatman glass fiber separator was placed on top to keep the electrode and Celgard from curling or folding before the cell assembly was finished. The cell was flooded with 1M $LiPF_6$ in 50/50 EC/DMC (Sigma Aldrich). $LiScMo_3O_8$ was cycled versus Li^+ using a BioLogic SP-200 potentiostat at a C/15 rate. A pattern was collected every 20 minutes during the discharge.

Electrochemical impedance spectroscopy Electrochemical impedance spectroscopy was performed on a BioLogic VSP potentiostat/galvanostat. Measurements were made on two-electrode coin cells between 1 MHz and 100 mHz using a 15 mV input. The cells were cycled at a C/20 rate, stopped at various amounts of Li^+ insertion, followed by collection of the impedance spectra.

X-ray photoelectron spectroscopy X-ray photoelectron spectroscopy samples were prepared by discharging/charging the cast electrodes outlined earlier to the desired voltages. The sample preparation methodology is described elsewhere.[?] All samples were measured using a Thermo Fisher Escalab Xi+ XPS equipped with a monochromatic Al anode (E=1486.7 eV). A cluster gun was used for 40 s to clean the surface and improve count intensity for all samples. Survey scans were measured at 100 eV pass energy, and high-resolution scans were measured in the Sc and Mo regions at 20 eV pass energy. *Ex situ* spectra were referenced to adventious carbon at 284.8 eV. CasaXPS was used to fit the data using Shirley backgrounds and GL(30) peak shapes. High resolution scans of Sc and Mo were fit using appropriate spin-orbit splitting and peak area ratios.

Raman spectroscopy Raman spectra were collected on a Horiba XploRA One confocal Raman microscope. All spectra were collected with a 638 nm diode laser, a diffraction grating with groove density 1200 gr mm^{-1}, and 1% laser power ($\approx$0.29 mW) to minimize laser damage to the electrode surface. The hole and slit were fixed at 500 and 50 μm, respectively. The laser was focused using a 50$\times$ (numerical aperture 0.50) objective, which

yielded a nominal spatial resolution of approximately 780 nm. *Operando* measurements were performed by focusing the laser on the front-side of the cathode in a custom spectro-electrochemical cell with a nylon body, stainless steel current collectors, and a borosilicate glass cover slip window (0.17 mm - 0.25 mm thickness). The cell stack was assembled with a slurry-cast electrode prepared as described previously, a Celgard 2400 separator with a 3/32" hole punched out, a polished Li foil anode with a 5/32" hole punched out, and 4 drops (65.8 $\pm$ 0.78 mg) of electrolyte. The electrolyte was the same composition as that used for the cycling experiments diluted by a factor of 10 to yield 0.1 M $LiPF_6$ to limit interference from fluorescence. Spectra were collected with a 3 s acquisition time and 200 accumulations continuously while the cell was cycled galvanostatically at $C/10$ based on 1 e^- between 1.2 V and 3 V. The microscope was refocused once during the experiment towards the end of the first charge cycle (i.e. after approximately 27 h).

Potentiometric entropy measurements   The open circuit voltage $U_{ocv}(x, T)$ and the entropic potential $\partial U_{ocv}(x, T)/\partial T$ of the coin cells with the $LiScMo_3O_8$ anode and lithium metal counter electrode were measured as functions of Li^+ composition x with a potentiometric entropy measurement technique using the apparatus described previously.[?] The potentiometric entropy measurements consisted of imposing a series of constant current pulses at a rate of C/10 for 30 minutes at 20 °C each followed by a relaxation period of 4.5 hours, ensuring that equilibrium had been reached and that $\partial U_{ocv}(x, T)/\partial T$ was less than 1 mV/h. During the relaxation period, a step-like temperature profile was applied to the coin cell from 15 °C to 25 °C in 5 °C increments with a thermoelectric cold plate (TE technology, CP-121). The temporal evaluation of the cell voltage was recorded with a potentiostat (Biologic, VSP-300). Before recording the open circuit voltage $U_{ocv}(x, T)$ and imposing the next temperature step, we verified that the cell had reached thermodynamic equilibrium by making sure that the temperature difference between the cold plate and the top of the coin cell was less than 0.1 °C and that the time rate of change of the open

circuit voltage $\partial U_{ocv}(x, T)/\partial T$ was less than 1 mV/h.

From the Nernst equation, the open circuit voltage $U_{ocv}(x, T)$ of the battery system is defined as[?]

$$U_{ocv}(x, T) = -\frac{\mu_{\mathrm{Li}}^{+}(x, T) - \mu_{\mathrm{Li}}^{-}(x, T)}{e} \tag{1}$$

Here, e is the unit charge and $\mu_{\mathrm{Li}}^{+/-}(x, T)$ is the Li^{+} chemical potential of the cathode (superscript "+") and anode (superscript "−"). By definition, $\mu_{\mathrm{Li}}^{+/-}(x, T)$ can be expressed as the partial molar Gibbs free energy, i.e.,[?]

$$\mu_{\mathrm{Li}}^{+/-}(x, T) = \frac{\partial g^{+/-}(x, T)}{\partial x} \tag{2}$$

where x is Li^{+} composition in the electrode and is defined as the fraction of the number of moles of Li^{+} N_{Li} intercalated per number of moles of molecular units of active material $N_{+/-}$ in the electrode such that $x = N_{\mathrm{Li}}/N_{+/-}$. Furthermore, under isobaric conditions, based on Maxwell's relations, the molar entropy of each electrode $s^{+/-}(T)$ can be expressed as[?]

$$s_{+/-}(x, T) = -\frac{\partial g_{+/-}(x, T)}{\partial T} \tag{3}$$

Thus, Based on the Clairaut's theorem, taking the derivative of Eq.(1) with respect to temperature T, the equation can be written in terms of the molar entropy $s^{+/-}(x, T)$, i.e.,

$$\frac{\partial U_{ocv}(x, T)}{\partial T} = \frac{1}{e}\left[\frac{\partial s_{+}(x, T)}{\partial x} - \frac{\partial s_{-}(x, T)}{\partial x}\right] \tag{4}$$

For the coin cells investigated in this study, the Li metal counter electrode was considered to be an infinite Li^{+} reservoir with no lattice rearrangement upon lithiation/delithiation.[?] Therefore, the partial molar entropy of Li^{+} metal electrode $\partial s^{\mathrm{Li}}(x, T)/\partial x$ can be assumed to be independent of x and constant when holding the temperature and pressure constant, i.e., $\partial s^{\mathrm{Li}}(x, T)/\partial x = s_{o}^{\mathrm{Li}}(T)$.[?][?] Therefore, the entropic potential of the coin cell can be

written as

$$\frac{\partial U_{ocv}(x, T)}{\partial T} = \frac{1}{e} \left[\frac{\partial s_{\mathrm{LSMO}}(x, T)}{\partial x} - s_{\mathrm{Li}}^{\mathrm{o}}(T) \right].$$ (5)

where superscripts "Li" and "LSMO" refer to the Li^+ metal counter electrode and $\mathrm{LiScMo_3O_8}$ working electrode respectively. Thus, the the measured $\partial U_{ocv}(x, T)/\partial T$ depends on the partial molar entropy of $\mathrm{LiScMo_3O_8}$ since $s_o^{\mathrm{Li}}(T)$ is independent of x. In other words, analyzing $\partial U_{ocv}(x, T)/\partial T$ measurements provides insights in the physicochemical phenomena occurring in the $\mathrm{LiScMo_3O_8}$ electrode.

Computational Methodology Mapping of the bond valence in the space of the crystal structure was carried out using the script PYABSTANTIA.[?]

Electronic structure calculations using density functional theory (DFT) were performed with the Vienna *ab initio* Simulation Package (VASP).[?,?,?,?] All calculations used projector augmented wave (PAW) pseudopotentials (Li sv, Sc sv, Mo sv, and O),[?,?] a plane-wave energy cutoff of 650 eV, and the SCAN meta-GGA exchange-correlation functional.[?,?] The Brillouin zone was sampled with Γ-centered Monkhorst-Pack meshes[?] of densities along each reciprocal lattice vector of 30 Å and 40 Å for total energy and density of states calculations, respectively. For total energy calculations, structures were relaxed using a force convergence criterion of 0.02 eV/Å and final static calculations were run using the linear tetrahedron method.[?] All calculations were spin-polarized, with ferromagnetic initialization of moments unless otherwise stated.

Symmetrically distinct Li^+-vacancy orderings in $\mathrm{Li}_x\mathrm{ScMo_3O_8}$ were enumerated using the Clusters Approach to Statistical Mechanics (CASM) software package.[?,?,?,?] All available tetrahedral and octahedral sites in the Li^+/Sc layer were considered for Li^+ occupation, except those sharing faces with the Sc sites, yielding two distinct tetrahedral sites and three equivalent octahedral sites per primitive cell. Additionally, we did not consider configurations with face-sharing between Li^+ sites. Energies were calculated for 295 configurations.

Voltage was calculated via the Nernst equation (Eq. 1), with the chemical potential of Li^+ metal in the body-centered cubic structure used as the reference anode chemical potential.

Supporting Information

The Supporting Information is available free of charge at [] with further details of the diffraction, impedance measurements, Raman spectroscopy, and calculated ground state configurations.

Acknowledgement

Graphical TOC Entry

Supporting Information for

Metal-Metal Bonding as an Electrode Design Principle in the Low-Strain Cluster Compound LiScMo$_3$O$_8$

Kira E. Wyckoff,[†] Jonas L. Kaufman,[†] Sun Woong Baek,[‡] Christian Dolle,[¶]

Joshua J. Zak,[§] Jadon Bienz,[∥] Linus Kautzsch,[†] Rebecca C. Vincent,[†]

Arava Zohar,[†] Kimberly A. See,[§] Yolita M. Eggeler,[¶] Laurent Pilon,[‡,⊥]

Anton Van der Ven,[*,†] and Ram Seshadri[*,†,∥]

†Materials Department and Materials Research Laboratory

University of California, Santa Barbara, California 93106, United States

‡Mechanical and Aerospace Engineering Department

Henry Samueli School of Engineering and Applied Science

University of California, Los Angeles, CA 90095, USA

¶Laboratory for Electron Microscopy, Microscopy of Nanoscale Structures and Mechanisms

Karlsruhe Institute of Technology, Engesserstr. 7, 76131 Karlsruhe, Germany

§Division of Chemistry and Chemical Engineering

California Institute of Technology, Pasadena, California 91125, United States

∥Department of Chemistry and Biochemistry

University of California, Santa Barbara, California 93106, United States

⊥California NanoSystems Institute and Institute of the Environment and Sustainability

University of California, Los Angeles, CA 90095, USA

E-mail: avdv@ucsb.edu; seshadri@mrl.ucsb.edu

Table 1: Summary of crystallographic refinement parameters from Figure 3 in the main text for LiScMo$_3$O$_8$ in space group $P3m1$ using synchrotron powder X-ray diffraction. The lattice parameters are $a = 5.7247$ Å and $c = 4.9436$ Å. B_{iso} is the thermal displacement parameter. The R-factors R_{wp} and R_{exp} are 14.12 and 7.05 respectively.

	Site	x	y	z	B_{iso} (Å^2)
Li1	$1c$	0.6667	0.3333	0.6140	1.0 (fixed)
Sc1	$1b$	0.3333	0.6667	0.71(8)	0.6(3)
Mo1	$3d$	0.8534	0.1466	0.24(1)	0.49(3)
O1	$1a$	0	0	0.50(6)	0.5(7)
O2	$1c$	0.6667	0.3333	0.01(5)	0.5(7)
O3	$3d$	0.4980	0.5020	0.46(0)	0.5(7)
O4	$3d$	0.1667	0.8333	0.00(3)	0.5(7)

Note: B_{iso} was fixed for Li at 1.0 Å^2. B_{iso} values for all of the O atoms were contrained to refine together.
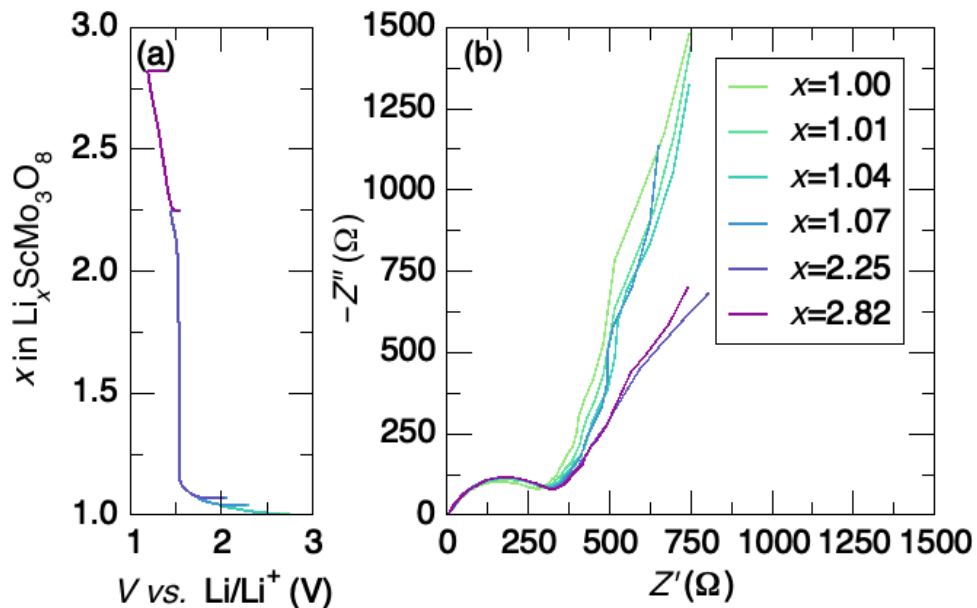
Figure 1: Electrochemical impedance spectra of slurry electrodes as a function of Li^+ content in $LiScMo_3O_8$. The charge transfer resistance remains relatively constant as a function of lithiation
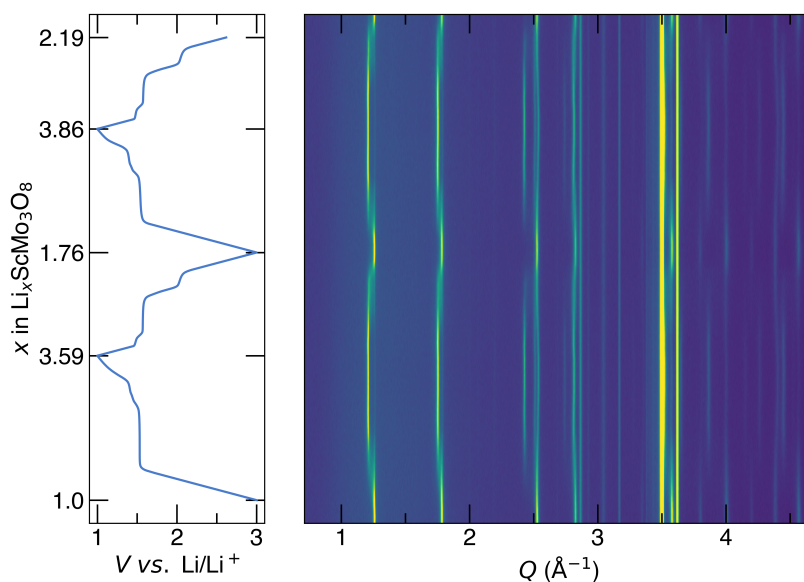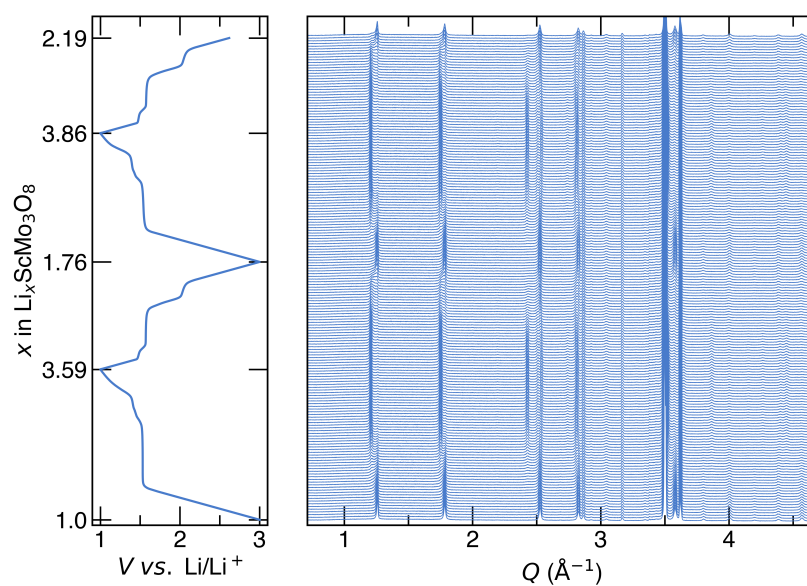

Figure 2: *Operando* X-ray diffraction of $LiScMo_3O_8$ during the first two galvanostatic discharge/charge cycles at a C/15 cycling rate. The electrochemistry is shown in the left-most panel, inserting over two additional Li^+ to $Li_3ScMo_3O_8$. The entire Q range is shown on the left as a heat map.

3

Figure 3: *Operando* X-ray diffraction of $LiScMo_3O_8$ during the first two galvanostatic discharge/charge cycles at a C/15 cycling rate. The electrochemistry is shown in the left-most panel, inserting over two additional Li^+ to $Li_3ScMo_3O_8$. The entire Q range is shown on the left.
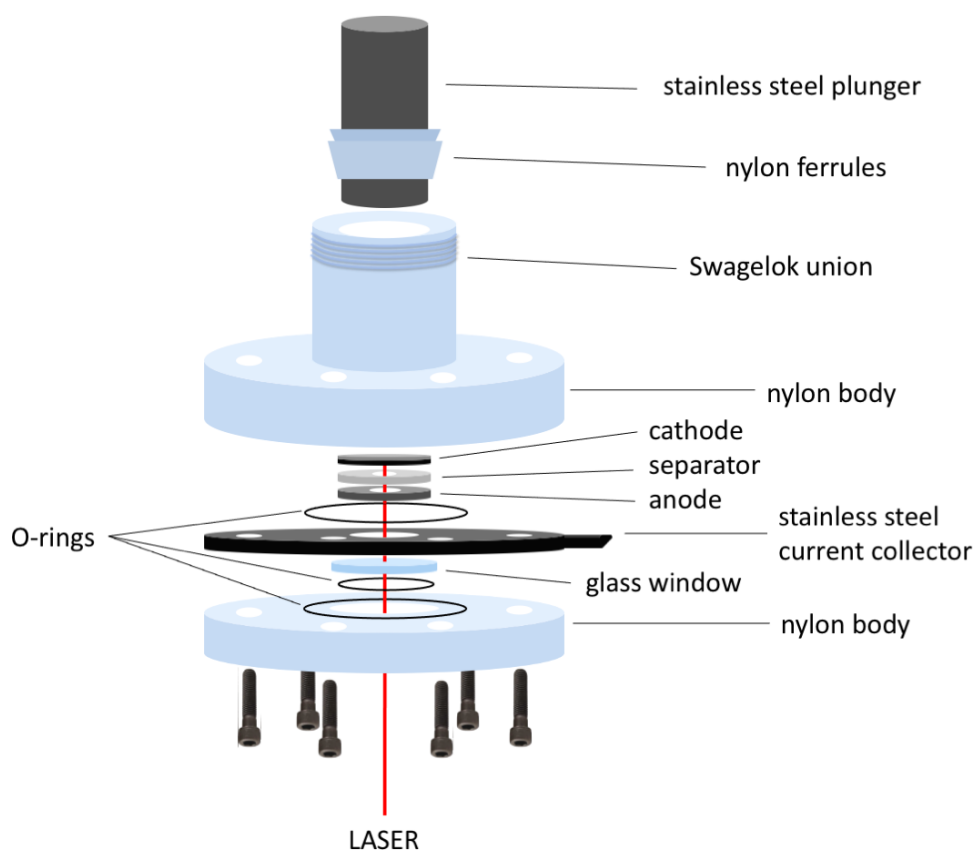
Figure 4: Schematic of custom spectroelectrochemical cell for *operando* Raman spectroscopy measurements in a front-side scattering arrangement with respect to the cathode.
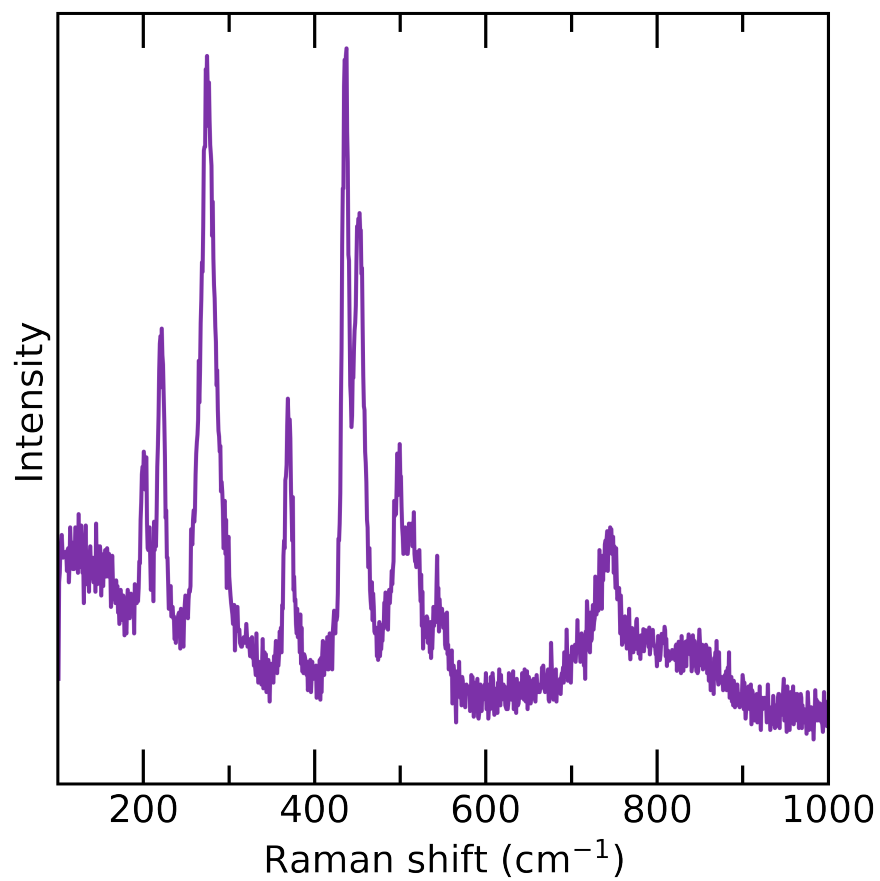
Figure 5: *Ex situ* Raman spectroscopy spectrum of pristine LiScMo$_3$O$_8$.

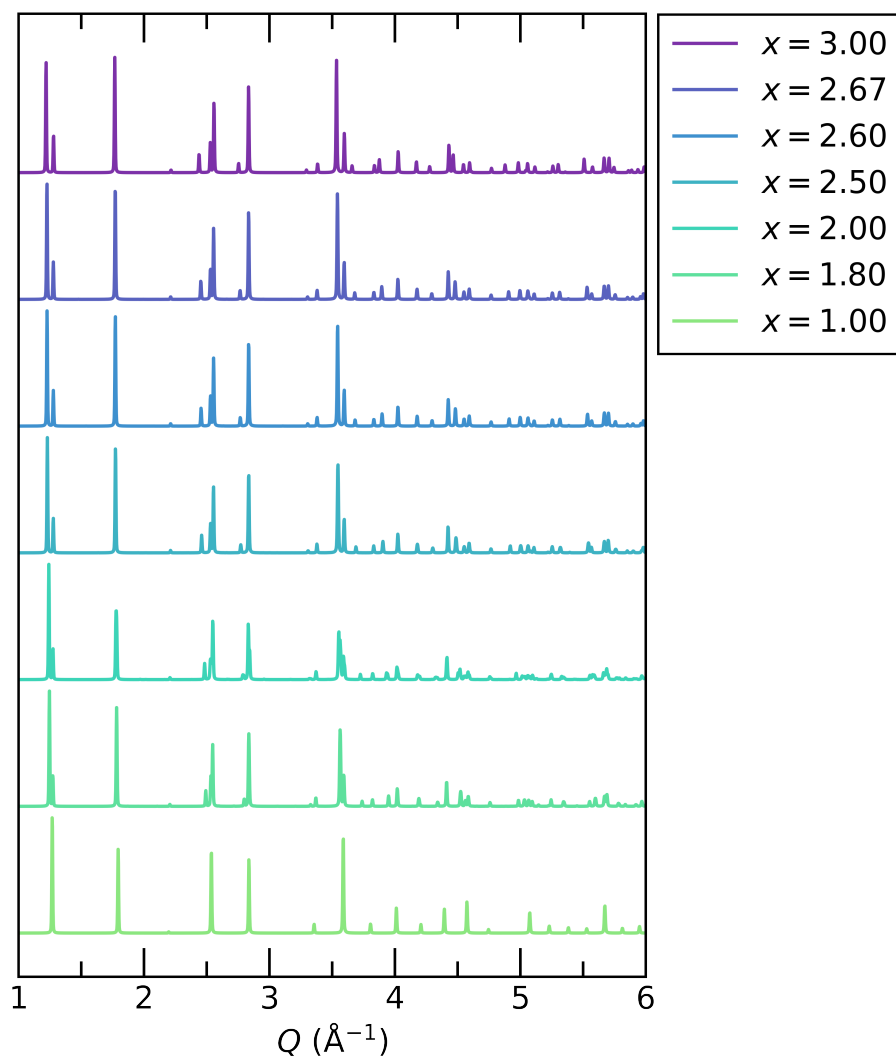Figure 6: Simulated diffraction data for ground state structures of $Li_xScMo_3O_8$ at $x = 1.00$, 1.80, 2.00, 2.50, 2.60, 2.67, and 2.85.
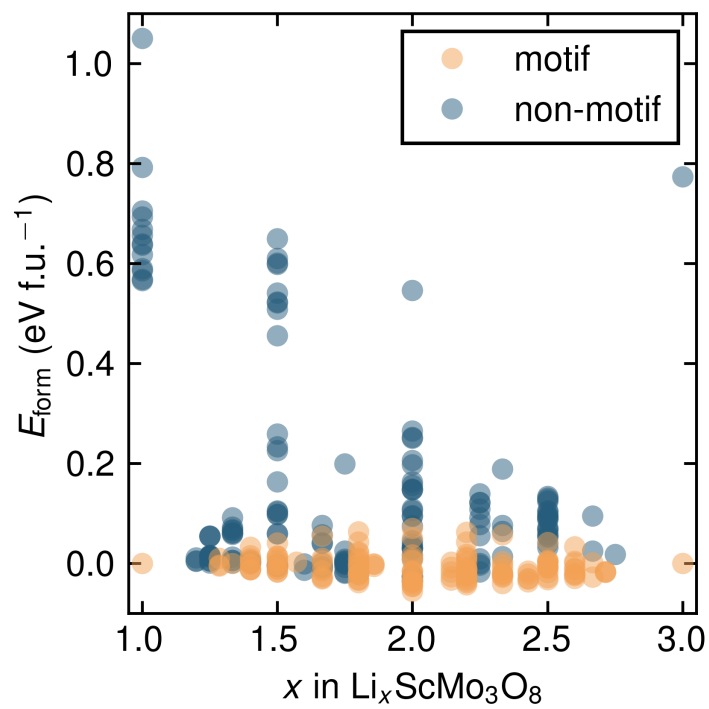
Figure 7: Calculated formation energies of distinct Li$^+$-vacancy orderings in Li$_x$ScMo$_3$O$_8$, labeled by whether the configuration follows the identified favorable Li$^+$ ordering motif.